This project has received funding from the European Union's Horizon 2020 research and innovation programme under grant agreement No 871813.

ICT Project No 871813

MUNDFAB

Modeling Unconventional Nanoscaled Device FABrication

D4.5: Report on the first version of atomistic studies and LKMC models

G. Calogero (CNR), D. Raciti (CNR), D. Ricciarelli (CNR), I. Deretzis (CNR), G. Fisicaro (CNR), A. La Magna (CNR), F. Cristiano (CNRS)

June 30, 2022

Quality management

This deliverable was reviewed by:

Paweł Michałowski, Łukasiewicz IMIF

Peter Pichler, Fraunhofer IISB

Contents

Executive Summary

This document reports on the first version of the super-Lattice Kinetic Monte Carlo atomistic models for the simulation of Laser Annealing (LA) processes in three-dimensional structures of arbitrary geometry. We introduce a hybrid computational scheme that allows combined use of atomic resolution for the particle kinetics (including phase changes from solid to liquid and *vice versa*) along with a continuum representation of the thermal and electromagnetic fields generated during the laser irradiation process. A preliminary version of the theoretical formalism has been presented in Deliverable D4.4 "Beta version of the laser-annealing models implementing a complete calibration of the optical and thermal properties for all the device materials", whereas here, extensions regarding technical and scientific aspects will be discussed, revealing the full potentiality of the computational code. Namely, software engineering tasks regarding the sharing of RAM between Python and Fortran modules will be deployed, giving the possibility to study extended defect formation during the LA process, as well as the kinetics of more complex materials, such as SiGe alloys. A novel KMC calibration scheme for the solid-liquid interface of SiGe materials with variable alloy fractions will be presented, along with relevant examples that demonstrate its applicability and relevance for LA processes. Finally, qualitative results from SiGe LA simulations will be presented, which highlight the potential enabled by the code improvements and KMC calibration.

1 Introduction

Pulsed Laser Annealing (LA) with pulses below 10 μs is a versatile and ultra-fast thermal annealing process that can be used for the manipulation of micro- and nano-electronic devices with complex geometries (1) (2). Simulations on LA are nowadays an integrated part of actual LA processes, as they allow to fine-tune the process parameters in order to achieve the requested process control in extremely confined spaces and timescales. Within this context, the MUNDFAB project has dedicated WP4 to the simulation of laser annealing. LA simulations are usually deployed by self-consistently solving electromagnetic heat equations along with phase-field equations, in order to topologically capture the melting phenomena and the respective phase changes over the laser-irradiated materials. The continuum nature of partial differential equations used to describe these processes allows for an accurate simulation of real processes (considering an exact matching of device geometries in the μm scale) with the aid of computational libraries that use finite element methods to solve the underlying mathematical problem. However, continuum fields do not allow to capture the local changes in the annealed materials with an atomistic resolution. This aspect can be very important, especially for microelectronic devices, as ultrafast phase changes in materials may generate point and extended defects than can be detrimental to device operation. In Deliverable D4.4 entitled "Beta version of the laser-annealing models implementing a complete calibration of the optical and thermal properties for all the device materials" we have introduced a novel methodology that simulates LA processes with an atomistic resolution. This methodology couples the electromagnetic heat equations solved through continuum approaches with an atomistic description of phase changes and the respective atom kinetics, using a super Lattice Kinetic Monte Carlo (LKMC) method. This "hybrid" methodology can, in principle, allow for the determination of all the local changes that take place during the LA process and reveal variations of substrate morphology resulting from the crystal-orientation-dependent atom kinetics, including structural imperfections, at the end of the thermal cycle. In D4.4 the code basic capabilities were demonstrated *via* LA simulations of a pure Si substrate. The code was completed in all its fundamental parts and the simulation results already showed interesting features which cannot be reliably obtained with a standard continuum approach (see Ref. (3)). The present deliverable, in addition to a brief summary of the theoretical background of the methodology, will deploy technical aspects that allow for the realization of the hybrid continuum/atomistic approach in computer systems with shared RAM through sockets connecting Python and Fortran modules and will disclose the full potentiality of the code, including examples of the formation of point and extended defects in laser annealed Si structures. Moreover, D4.5 will present a new calibration scheme for the solid/liquid interface of SiGe alloys with variable alloy fractions. We note that SiGe simulations are at the basis of many MUNDFAB WPs, as SiGe alloys have composition-dependent structural, electrical, and optical properties, whereas they preserve a key role for future microelectronics. Preliminary examples of SiGe LA simulations, based on the aforementioned KMC calibration, will also be discussed, with an emphasis on the importance of enabling shared RAM to carry them out.

2 The atomistic laser annealing method

The Atomistic Laser Annealing method was recently developed within the MUNDFAB project by the CNR group and formally presented to the scientific community in Ref. (3). It can describe phase transitions occurring during LA processes for group IV elemental semiconductors (Si, Ge) or alloys (SiGe), with an atomistic resolution. It is based on a multi-scale self-consistent procedure that couples a continuum, finite-elements model (FEM) for µm-scale temperature diffusion with the super-lattice Kinetic Monte Carlo scheme implemented in the MulSKIPS code, developed by the CNR (https://github.com/MulSKIPS/MulSKIPS). The computational procedure is based on a parallel coupling between the continuum and the atomistic models, contrary to sequential coupling approaches, where the thermal problem is first solved over the whole pulse duration via, e.g., a phase-field formalism, while coupling with the LKMC occurs only afterward. Here instead, the procedure starts by generating the FEM mesh from a user-provided CAD structure, containing information about regions to be modeled by the LKMC. Then, the temperature field in the FEM model is found at every user-defined time step Δt by solving the usual coupled partial differential equations for the LA-induced heating until the melting temperature is locally reached for the irradiated material. Thereafter an iterative procedure begins for each time step, which for the entire pulse duration couples the FEM and LKMC simulators in the following way: (a) the temperature field is calculated by solving the continuum equations of heat over the entire FEM mesh, whereas results are interpolated into a (much denser) Monte Carlo super-lattice; (b) the non-homogeneous temperature map found from step (a) is used to compute the solidification/melting probabilities of each site in the LKMC super-lattice, which are then used to simulate the kinetic evolution of the solid-liquid interface over Δt; (c) the atoms that underwent a phase change during the LKMC simulation are communicated to the FEM model, which again solves the LA thermal problem while accounting for this variation; (d) the procedure restarts from step (a) and goes on for the whole pulse duration until all atoms in the structure have recrystallized. With this approach, the absorbed or released latent heat at each time step can be exactly computed by directly integrating the melt (recrystallized) volume during the LKMC simulations over Δt.

Within the atomistic KMC framework, in the case of a homogeneous material such as pure Si or Ge, the solid-liquid interface is regulated by the balance between solidification and melting events, whose rates are expressed as (4) (5):

$$\nu_{ls} = \nu_{ls}(\boldsymbol{r}, t) = \nu_0 \cdot f(T) \cdot e^{-\frac{2 \cdot E_n}{k_B T_M}}$$

$$\nu_{sl} = \nu_{sl}(\boldsymbol{r}, t) = \nu_0 \cdot e^{-\frac{n \cdot (\Phi_S - \Phi_L)}{k_B T(\boldsymbol{r}, t)}}$$

where ν_0 is a constant prefactor, T_M is the melting temperature, n is the number of bonds that an interface site forms with atoms in the solid phase, Φ_S – Φ_L is the difference between the bond energy of two Si (Ge) atoms binding in the solid (Φ_S) and liquid phases (Φ_L) (6), E_n is the energy barrier needed to solidify a liquid Si (Ge) atom in an n-coordinated LKMC site, with $E_{n=2}$ fixed to Φ_S – Φ_L to ensure equilibrium for a flat interface at T=T$_M$, while $E_{n=1}$, $E_{n=3}$, ν_0 and

$$f(T(\boldsymbol{r}, t)) = \frac{1}{2}\left[1 + erf\left(\frac{T(\boldsymbol{r}, t) - T_{FV}}{W_{FV}}\right)\right]$$

are chosen to reproduce the analytical Fulcher-Vogel relationship for the interface speed as a function of T fitted via experimental data (7). Such an expression is approximately linear close to $T = T_M$, it has a maximum in the under-cooling region ($T < T_M$) and monotonically increases in absolute value for $T > T_M$.

A generalization of such calibration for a complex alloy such as SiGe will be introduced in Section 3.

The computational implementation of this approach is based on two distinct modules of the MulSKIPS code (a Python module solving the partial differential equations of the thermal field on a FEM mesh, and a Fortran module implementing advanced LKMC algorithms for the atom kinetics and the evolution of the solid/liquid interface). In order to show its full potentiality (including the capability to generate point and extended defects during the LA process simulation, but also track the space/time variations of material composition needed, e.g., to capture Ge segregation in SiGe), the code requires that these two modules operate on a shared RAM of a computational platform. The technical aspects and some paradigms of this code development will be discussed in the next paragraph.

2.1 Sharing RAM in atomistic LA simulations

The major technical improvement of enabling shared RAM, and thus efficient in-memory data transfers, between the Fortran KMC and the Python continuum FEM environments for LA simulations was achieved by integrating the so-called "F2Py sockets" into the MulSKIPS code, generalizing some of the routines available here: https://github.com/b-fg/f2py-sockets. The workflow after full integration of F2Py functionalities in the Python and Fortran MulSKIPS modules is outlined in **Figure 1**.

2.1.1 F2Py sockets implementation in MulSKIPS

During a hybrid KMC/FEM LA simulation three key data transfers are carried out between the Fortran and Python solvers, one at the beginning of the simulation and the others at every time step Δt. The first one is a geometry transfer from Python to Fortran, occurring after interpolation of the relevant part of CAD mesh into the MulSKIPS superlattice formalism. The second one is the thermal field transfer from Python to Fortran at every time step Δt, which is used as input in MulSKIPS to determine the KMC space- and time-dependent melting/solidification event probabilities. The third one is the solid/liquid phases transfer from Fortran to Python at every time step Δt, which is used to get the phase-changed volume in the FEM model and compute the exchanged latent heat needed to solve the Maxwell-Fourier self-consistent problem, and get an updated thermal field in the following iteration. Before implementing F2Py sockets, such data (in the form of arrays with KMC superlattice dimension $L_x \times L_y \times L_z$) used to be transferred from Python to Fortran and *vice versa* by means of heavy write/read operations on disk, with obvious performance limitations and demanding storage requirements (e.g., each of the simulations reported in Deliverable D4.4 involved hundreds of HD I/O operations on temporary data files in the order of 1 GB each). F2Py sockets allow performing such array transfers directly in the RAM, without involving any disk operation.

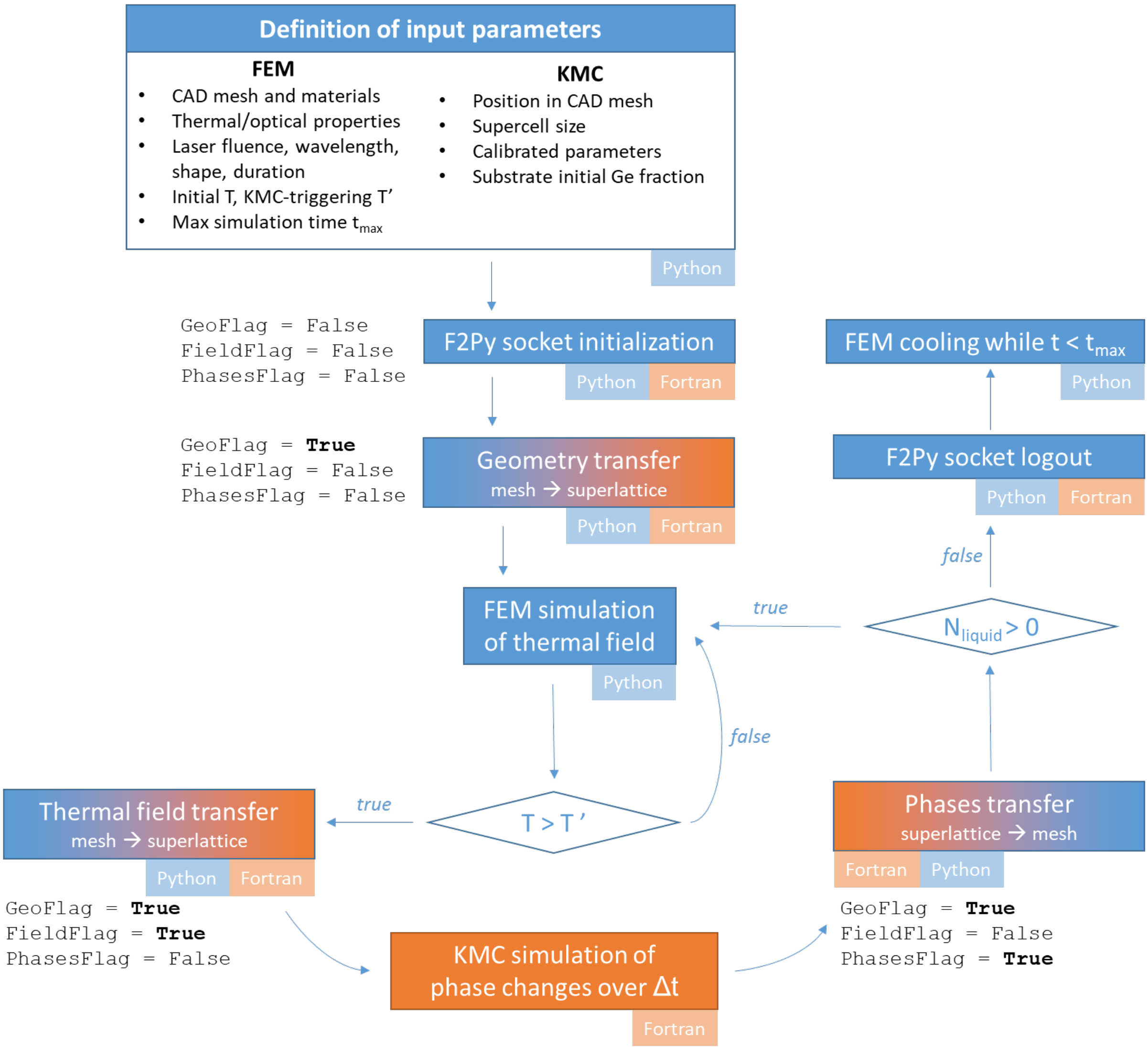

Figure 1 – Schematics of the LA simulation workflow, clearly indicating the steps which involve F2Py sockets. The three control flags GeoFlag, FieldFlag, and PhasesFlag are used in Fortran to indicate the availability in RAM of the corresponding data arrays and trigger the communications between Fortran and Python.

From a more technical point of view, the operations involving F2Py sockets are performed by ad-hoc “send” and “receive” routines implemented in both Fortran and Python environments, whose execution is triggered in Fortran by proper combinations of the three control flags GeoFlag, FieldFlag and PhasesFlag, each indicating the availability in RAM of the geometry, thermal field and phases data arrays, respectively (we note that fields other than temperature could be used, in principle, to set up MulSKIPS probabilities using such a multiscale coupling workflow). The initialization of the F2Py socket and the MulSKIPS unique Fortran CPU process is carried out right after setting up the LA simulation parameters in Python. At the beginning of the Fortran CPU process, all flags are set to False, meaning that the KMC code is on standby and waiting for instructions from Python. The Python module interpolates a local mesh region into a data array in the form of superlattice sites occupations, issues a “send” command to communicate the geometry information *via* the F2Py socket, and is put on standby. The “send” command in Python triggers a “receive” command in Fortran, which reads the data array stored in RAM by Python, uses them to set up the superlattice occupations, then sets the GeoFlag to True and is put in standby. In the latter step, the original number of each atomic species is also stored, as a reference to ensure mass conservation during solidification at the latest stages of the LA simulation. The Python module enters the FEM cycle and heats up the system by simulating laser absorption until the maximum temperature in the mesh reaches a trigger temperature *T’* (e.g., the melting temperature in the case of elemental semiconductors like Si or Ge). At this point, the thermal field is interpolated and sent to Fortran *via* F2Py sockets, which receive it and set the FieldFlag to True. This last statement, combined with the True state of GeoFlag, triggers the setup of KMC probabilities and marks the beginning of the first KMC cycle. Once the KMC simulated time interval reaches Δt, the solid/liquid state of each superlattice site is stored in RAM, a “send” command is issued (this time in Fortran), the PhasesFlag is set to True and the FieldFlag is restored to False, ensuring that the Fortran CPU process stays in standby until a new thermal field is transferred. Python reads such phases from RAM, uses them to update the liquid and solid volumes in the mesh, and recalculates the thermal field. As this sequence goes on, the number of liquid and solid sites in the KMC superlattice is continuously tracked in the Fortran environment, differentiating the various chemical species (e.g., Si and Ge in SiGe alloys). Once the original number of solid species is recovered (or, equivalently, there are no more liquid sites) the solid phases from Fortran are communicated one last time to Python and the F2Py connection is closed. At this point, the FEM cooling cycle continues until the maximum simulation time t_{max} set up at the beginning of the LA simulation is reached.

2.1.2 Test applications: defects and species tracking

In addition to optimizing data exchange, an F2Py socket allows for the execution of a *unique* MulSKIPS CPU process for the whole LA simulation (rather than a sequence of independent MulSKIPS CPU processes initialized at every time step Δt). This in turn means that the information about KMC sites’ occupations and coordinations can be retained across subsequent KMC-FEM communication cycles. Such operation was previously unfeasible because MulSKIPS needed to be reinitialized after every FEM step, causing an inevitable reset of MulSKIPS superlattice information. This has the important advantages of unlocking the simulation of defects in the irradiated material, which is a native characteristic feature of MulSKIPS, as well as tracking the concentration and position of every solid species within the KMC box during the LA simulation.

In MulSKIPS the formation and evolution of both point and extended defects can be accounted for during a LA process simulation (solidification), owing to the superlattice nature of the code itself. The number of defects formed is generally higher whenever the process-specific kinetics is such to destabilize higher-coordinated solid sites in favor of lower-coordinated ones. Vacancies can form whenever a void gets surrounded by four three-coordinated solid sites. Furthermore, every time a solid site in MulSKIPS has coordination equal to one, a choice is made in the code to fix the stacking configurations for its possible nearest neighbors. The preference towards a stacking choice or another can be tuned by means of an input parameter (called PtransZig) ranging from 0 to 1, with the latter leading to non-defective stacking (see Ref. (8) for a detailed description of such parameter and its effects on the generation of defective structures). RAM storage through F2Py sockets allows preserving the information about vacancies positions in the KMC box across subsequent KMC cycles, which would otherwise be lost whenever MulSKIPS is reinitialized from scratch at every Δt. More importantly, it makes it possible to keep the information about stacking choices made for all one-coordinated solid sites across subsequent KMC Δt-long cycles, enabling the evolution of extended defects or differently oriented grains during the LA-induced resolidification.

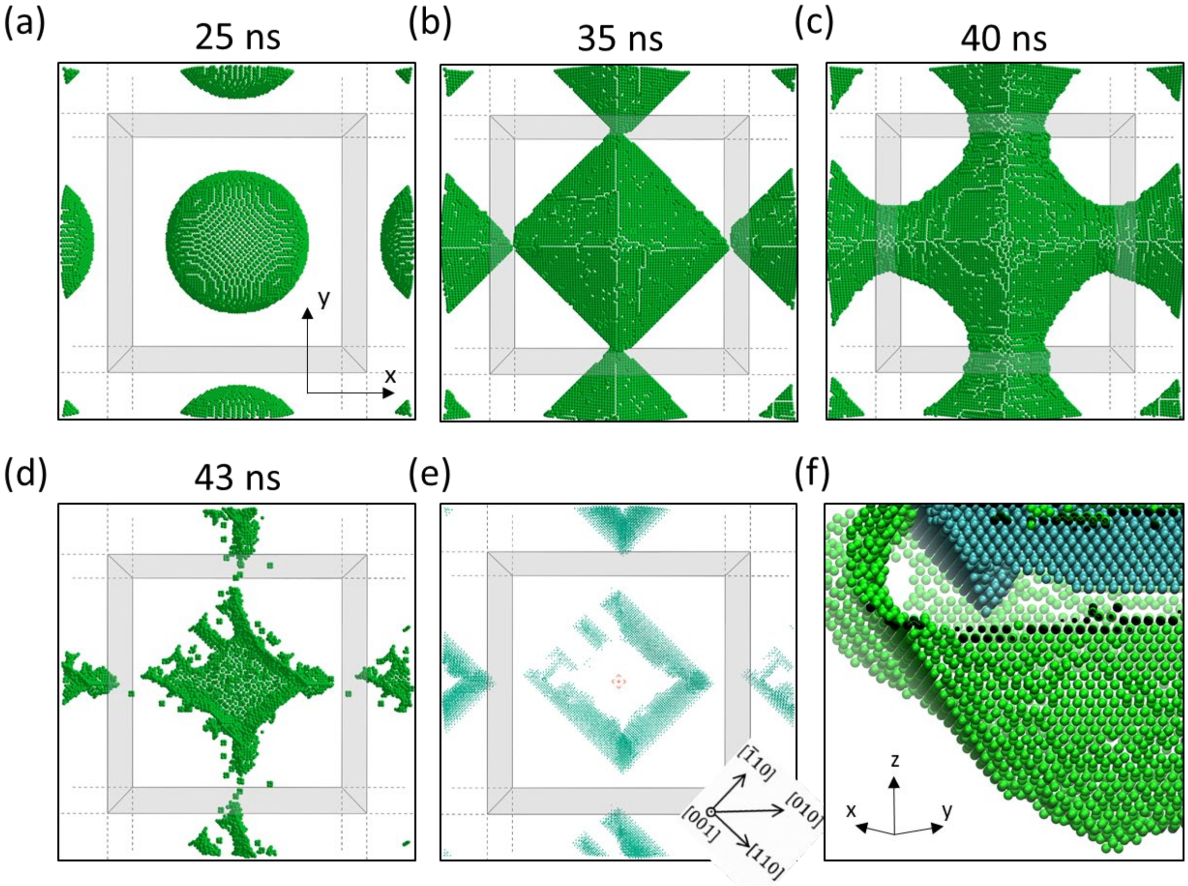

Figure 2 – Example of defective LA simulation of a Si(001) surface. a-e) bottom view snapshots of the solid-liquid interface (green) at various instants of an LA simulation carried out with pulse fluence of 1.13 J cm-2, pulse duration of 20 ns, wavelength 308 nm, and assuming inhomogeneous nucleation with initial liquid hemispherical nuclei of 7 nm radius. Periodic images of the KMC box along x and y are also shown. f) Close view of differently oriented grain (light blue), overlapped with the partially [111] faceted solid-liquid interface existing in the KMC box at 40 ns. Formation and tracking of point defects, as well as the evolution of differently oriented Si grains, could be modeled thanks to the usage of F2Py sockets in MulSKIPS.

As an example, in **Figure 2** we report several snapshots (bottom views) of the evolving solid-liquid interface from one of the LA simulations for Si(001) with inhomogeneous nucleation described in **Deliverable D4.4, Section 1.2 (Figure 10)**, namely one carried out with pulse fluence of 1.13 J cm^{-2}, pulse duration of 20 ns, the wavelength of 308 nm and initial liquid hemispherical nucleus of 7 nm radius. Contrary to the simulation shown in **Deliverable D4.4**, in this case, a quite low PtransZig=0.5 was set, to maximize the formation of defects and highlight the capabilities that were unlocked in the code thanks to the usage of F2Py sockets. While this has no significant consequences in the melting stage of the LA simulation (**Figure**

2a-c), which yields the typical [111] faceting and partial nuclei coalescence phenomenon already discussed in **Deliverable D4.4** and Ref. (3), it does have an important effect on the way silicon solidifies afterward. In **Figure 2d**, one may notice indeed that several point defects were formed during the rapid solidification. Using F2Py sockets it was possible to keep the information about their position in the KMC box from the onset of solidification all the way to total solidification, across subsequent KMC cycles of Δt = 0.5 ns. In addition to this, Si grains with different orientations could also generate and evolve during the latest stages of solidification. In **Figure 2e** a bottom view of a differently oriented Si grain is reported, whereas in **Figure 2f** a zoom-in view of such grain is shown in light blue, along with the partially [111] faceted solid-liquid interface existing in the KMC box at 40 ns since the beginning of laser irradiation.

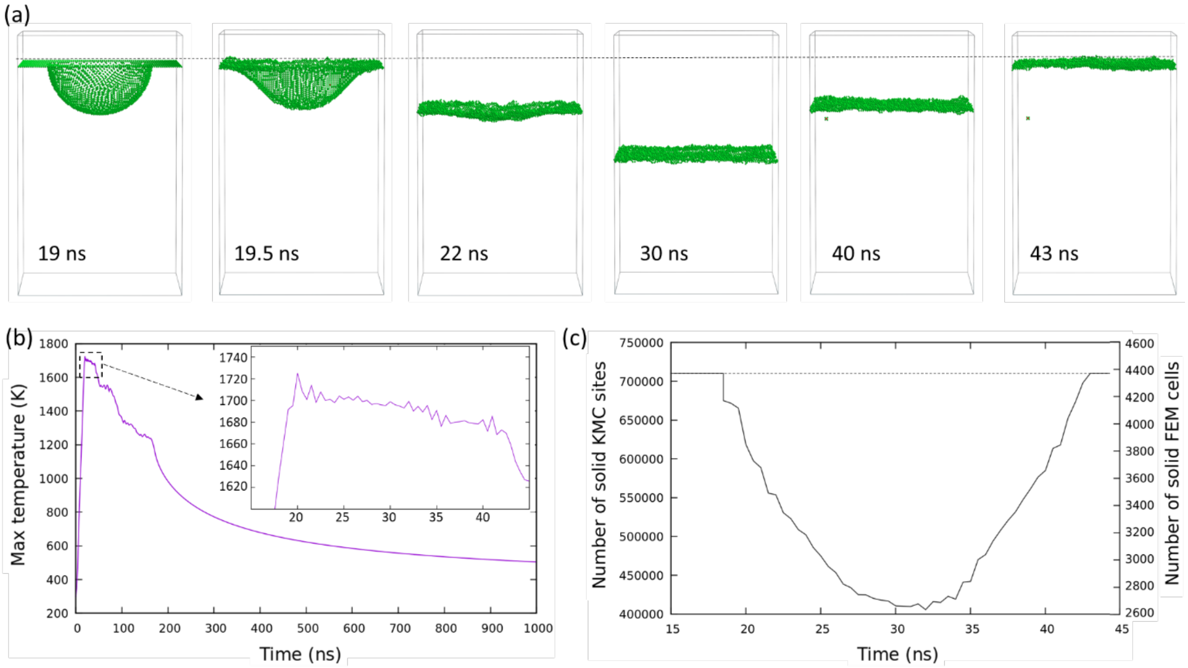

Figure 3 – Example of LA simulation for Si(001) with species tracking and ensured mass conservation enabled by sharing RAM. A fluence of 1.13 J cm-2, pulse duration of 20 ns, the wavelength of 308 nm, initial liquid nucleus radius of 7 nm, and PtransZig=1.0 were used, modeling laser absorption over the entire Si surface. (a) Snapshots of the solid-liquid interface at various instants of the simulation. (b) Maximum temperature in the FEM mesh as a function of time. (c) Number of solid Si sites within the KMC box (left axis) and within the FEM mesh (right axis) as a function of time.

Another example, highlighting the benefits of sharing RAM, is described in **Figure 3**. Here an LA simulation similar to the previous one was carried out, same box size and pulse properties, but with PtransZig=1.0 (no stacking defects formation, only vacancies) and modeling a case where the whole Si(001) top surface can interact with the laser pulse and undergo melting and subsequent solidification. We indeed note that the simulation in **Figure 2** modeled a situation where the laser pulse interacts with the initial liquid hemispherical nucleus only, leaving the surrounding flat Si surface untouched, as if it was covered with an inert optically reflective mask. Thanks to the usage of F2Py sockets it was possible to monitor the number of solid sites at every instant of the simulation and ensure that the solidification ends whenever the original number of solid sites is recovered. In **Figure 3a**, a sequence of snapshots of the solid-liquid interface is shown, while in **Figure 3b-c** the maximum temperature in the mesh and the number of solid Si sites in the KMC box (and the corresponding ones in the mesh) are plotted over time. The substrate before melting is completely flat at the position indicated by the dotted line in **Figure 3a** contains a total of 710.400 solid Si sites. At 19 ns from the beginning of irradiation, the maximum temperature overcomes locally the melting temperature of Si, and a liquid hemispherical nucleus is first generated in the KMC box. As time runs, the (001)-oriented solid-liquid interface surrounding the nucleus melts faster than the nucleus itself, until at 22 ns a roughly flat interface is left, indicating the formation of a rather homogeneous liquid layer on top of the residual solid substrate. When the maximum melt depth is reached, at around 30 ns, the number of solid Si sites has decreased to roughly 400.000 units. Then solidification begins and this number increases, as expected until the initial number of solid sites is recovered (see **Figure 3c**). Interestingly, from the latest snapshots in **Figure 3a**, one may also note that a vacancy was formed during solidification and the information about its position could be kept across several FEM-KMC cycles, until the end of the solidification. While in reality, thermal fluctuations would probably quickly annihilate such point defects, this demonstrates once again that the new version of the code is able to handle the formation and evolution of defective configurations during a LA process.

Such new species tracking capability, besides ensuring mass conservation at the end of solidification in the LA simulation, is of uttermost importance to estimate how Ge concentration varies over space and time in SiGe alloy LA process simulations, where the Ge fraction in liquid mostly determines the kinetics of atoms at the solid-liquid interface, and where analyzing the Ge concentration profile at the end of irradiation can be critical to validate the simulations against experiments.

3 KMC calibration for $Si_{(1-x)}Ge_x$ alloy melting-solidification

In this section we report on the application of the updated LA code to the melting-solidification processes of $Si_{(1-x)}Ge_x$ alloys, focusing on the calibration approach.

The calibration of Si-Ge mixtures is based on the single-species calibrations of pure Si and Ge. As previously discussed for the case of Si [see MUNDFAB Deliverable D4.4 and Ref. (3)], the evolution of the solid-liquid interface in the MulSKIPS LKMC code is regulated by the balance between solidification and melting events. The form of the event rates adopted for $Si_{(1-x)}Ge_x$ will be discussed below in this section.

Notice that the single-species solidification-melting process simulations were calibrated against the Fulcher-Vogel relation (1) (9) for the pure (crystalline) species, which gives the temperature dependence of the interface velocity [see MUNDFAB Deliverable D4.4 and Ref. (3)]. No such relations exist in the case of alloys. On the contrary, we relied on the experimental phase diagram of the material, expressing the temperature-dependent composition of the solid and the liquid phases at equilibrium, when the melting/solidification process is operated at a very slow speed.

The phase diagram of the solid-liquid Si-Ge system is well known from the literature (10) (see **Figure 4, panel A**). The behavior of the alloy is very close to ideal (Raoultian) (10) (11), where enthalpic contributions to the mixing energy are negligible and the lens shape of the diagram mostly depends on the entropy of fusion of the component species (the larger the entropy, the broader the shape).

3.1 Calibration strategy

Prior to Si-Ge alloys, we calibrated the solidification-melting KMC process for pure Ge. The probability equations for the solidification (“ls”) and melting (“sl”) MC events take the same form as that described for the case of pure Si (see MUNDFAB Deliverable D4.4 and Ref. (3)) and are comprised in the formulation adopted for Si$_{(1-x)}$Ge$_x$ in the more general SiGe PyMulSKIPS class (see D3.4, Section 3.2.2).

For the case of Si$_{(1-x)}$Ge$_x$, a few assumptions were made. The KMC event probabilities were defined assuming the Raoultian behavior of the mixture, as justified above. Concerning the simulation set-up, the liquid phase surmounting the solid material is assumed to have a fixed composition $(1 - x_L,\ x_L)$ in (Si,Ge), meaning negligible diffusion times of Si and Ge atoms within an infinite liquid reservoir. Moreover, the temperature is kept constant and uniform in the simulation box at every KMC run. Importantly, the condition on the uniformity of temperature and composition in space and time is assumed for calibration purposes only and is dropped in actual KMC LA simulations.

The MC event probabilities for species *i* (*i*=Si,Ge) read:

- *Solidification*:

$$\nu_{ls}^i = X^i \cdot \nu_0^i \cdot e^{-\frac{2E_{ls}^i(n)}{k_B T_m^i}} \cdot f(i,T) \tag{1}$$

where ν_0^i and $E_{ls}^i(n)$ are the Boltzmann prefactor and the energy barriers (dependent on the coordination number n, see **Table 1**) for the species i; $f(i,T) = \frac{1}{2}\left[1 + erf\left(\frac{T-T_0^i}{A^i}\right)\right]$ is a damping factor; T_m^i is the melting temperature of i. Notice that all these parameters were obtained from the calibration of pure Si and Ge melting-solidification kinetics against the respective Fulcher-Vogel curve. Finally, $X^i = 1 - x_L$ for Si and $X^i = x_L$ for Ge in the assumption of fast diffusion and of an infinite reservoir of liquid.

Table 1 - Solidification energies for Si (left column) and Ge (right column). The energy values coincide with those used in the single-species calibrations.

$\boldsymbol{E_{ls}^{Si}(1) = (E_2^{Si} - \delta^{Si})}$ $\boldsymbol{E_{ls}^{Si}(2) = E_2^{Si}}$ $\boldsymbol{E_{ls}^{Si}(3) = (E_2^{Si} + \delta^{Si})}$	$\boldsymbol{E_{ls}^{Ge}(1) = (E_2^{Ge} - \delta^{Ge})}$ $\boldsymbol{E_{ls}^{Ge}(2) = E_2^{Ge}}$ $\boldsymbol{E_{ls}^{Ge}(3) = (E_2^{Ge} + \delta^{Ge})}$

- *Melting*:

$$\nu_{sl}^i = \nu_0^i \cdot e^{-\frac{n\, E_{sl}^i(n_{Si}, n_{Ge})}{k_B T}} \tag{2}$$

where ν_0^i is defined as in the solidification case and $E_{sl}^i(\mathrm{n_{Si}}, \mathrm{n_{Ge}})$ are the melting energy barriers (equivalent to bonding energies), that depend on the number and kind of nearest neighbors ($n_{Si} + n_{Ge} = n$). The definition of $E_{sl}^i(\mathrm{n_{Si}}, \mathrm{n_{Ge}})$ is crucial for the calibration. Under the assumption of ideal (Raoultian) mixing, which holds for the case of Si-Ge alloys, the energy ε_{ij} of a mixed bond can be estimated as $\varepsilon_{ij} = (\varepsilon_{ii} + \varepsilon_{jj})/2$. An initial guess for the values of $E_{sl}^i(\mathrm{n_{Si}}, \mathrm{n_{Ge}})$ is therefore obtained as linear combinations of the solidification energy barriers for pure Si and Ge, $E_2^{Si} \equiv E_{ls}^{Si}(2)$ and $E_2^{Ge} \equiv E_{ls}^{Ge}(2)$, weighed on the number of Si and Ge nearest neighbors. The energy barriers for mixed bonding states are perturbed (i.e., further decreased in the case of Si and increased in the case of Ge) by a small amount to reproduce the experimental phase diagram of the alloy. The resulting 18 energy parameters (9 for Si and 9 for Ge) take the form reported in **Table 2**. For the sake of simplicity, at this stage of the study the perturbation was chosen to be the same for every coordination state of Si (α) and Ge (β), reducing the calibration to two parameters only.

Table 2 - Melting energies $E_{sl}^{i}(n_{Si}, n_{Ge})$ for i=Si (left column) and i=Ge (right column).

$\boldsymbol{E_{sl}^{Si}(1,0) = E_2^{Si}}$	$\boldsymbol{E_{sl}^{Ge}(1,0) = (1+\beta)\left[E_2^{Ge} + E_2^{Si}\right]/2}$
$\boldsymbol{E_{sl}^{Si}(0,1) = (1-\alpha)\left[E_2^{Si} + E_2^{Ge}\right]/2}$	$\boldsymbol{E_{sl}^{Ge}(0,1) = E_2^{Ge}}$
$\boldsymbol{E_{sl}^{Si}(1,1) = (1-\alpha)\left[3E_2^{Si} + E_2^{Ge}\right]/4}$	$\boldsymbol{E_{sl}^{Ge}(1,1) = (1+\beta)\left[3E_2^{Ge} + E_2^{Si}\right]/4}$
$\boldsymbol{E_{sl}^{Si}(2,0) = E_2^{Si}}$	$\boldsymbol{E_{sl}^{Ge}(2,0) = (1+\beta)\left[E_2^{Ge} + E_2^{Si}\right]/2}$
$\boldsymbol{E_{sl}^{Si}(0,2) = (1-\alpha)\left[E_2^{Si} + E_2^{Ge}\right]/2}$	$\boldsymbol{E_{sl}^{Ge}(0,2) = E_2^{Ge}}$
$\boldsymbol{E_{sl}^{Si}(2,1) = (1-\alpha)\left[5E_2^{Si} + E_2^{Ge}\right]/6}$	$\boldsymbol{E_{sl}^{Ge}(2,1) = (1+\beta)\left[2E_2^{Ge} + E_2^{Si}\right]/3}$
$\boldsymbol{E_{sl}^{Si}(1,2) = (1-\alpha)\left[2E_2^{Si} + E_2^{Ge}\right]/3}$	$\boldsymbol{E_{sl}^{Ge}(1,2) = (1+\beta)\left[5E_2^{Ge} + E_2^{Si}\right]/6}$
$\boldsymbol{E_{sl}^{Si}(3,0) = E_2^{Si}}$	$\boldsymbol{E_{sl}^{Ge}(3,0) = (1+\beta)\left[E_2^{Ge} + E_2^{Si}\right]/2}$
$\boldsymbol{E_{sl}^{Si}(0,3) = (1-\alpha)\left[E_2^{Si} + E_2^{Ge}\right]/2}$	$\boldsymbol{E_{sl}^{Ge}(0,3) = E_2^{Ge}}$

Notice that in the FEM-LKMC simulations the MC frequencies ν_{ls}^{i} and ν_{sl}^{i} reported above depend on both the time t and the lattice position $\boldsymbol{r}$. Indeed, both the temperature $T \equiv T(\boldsymbol{r}, t)$ and, eventually, the liquid-phase composition $x_L \equiv x_L(\boldsymbol{r}, t)$ (i.e., the parameter X^i) vary along the simulation, and are mapped from the FEM outputs obtained at every time step.

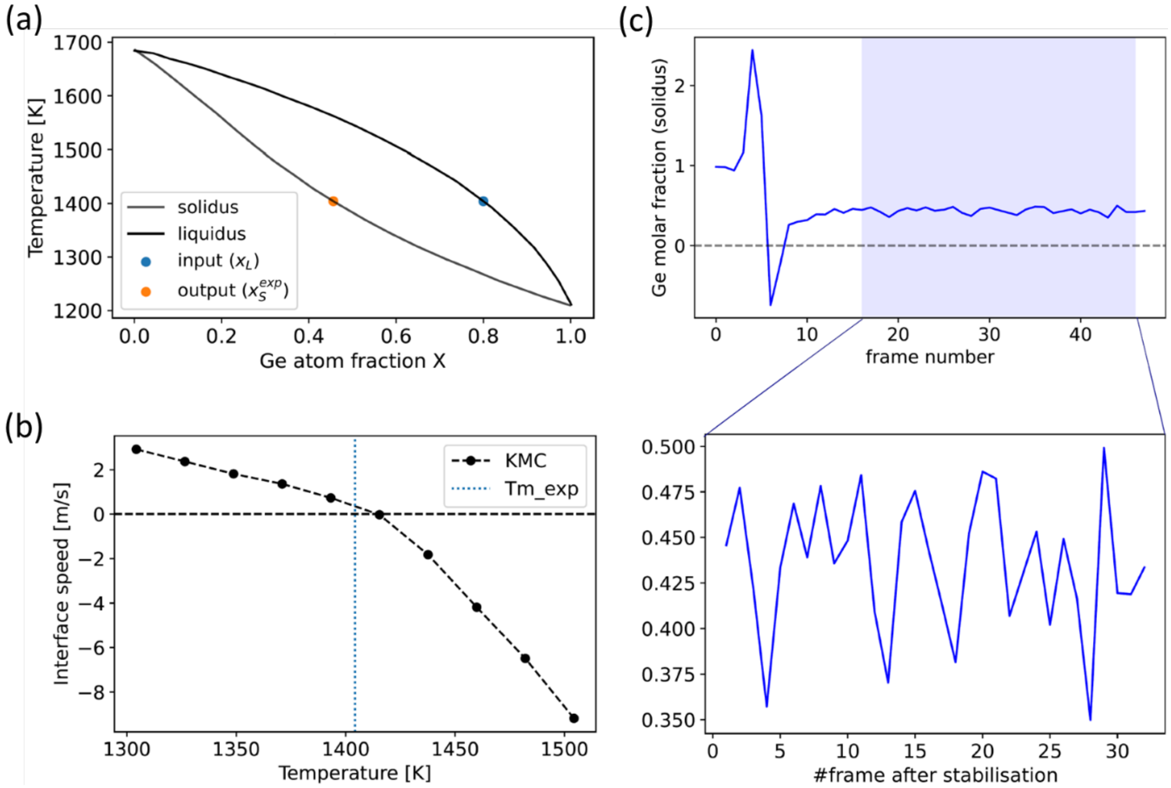

Figure 4 - Some steps of the calibration workflow for the case of $x_L = 0.8$. (a): experimental (T,x_{Ge}) solid-liquid phase diagram of the Si-Ge mixture; the x_L value on the liquidus *curve is marked in blue, the expected x_S value on the* solidus *curve (0.46 in this case) is marked in orange. (b): temperature-dependent interface velocity v(T) predicted from the KMC model (black line-scatter) vs expected equilibrium temperature for the given x_L from the experimental phase diagram (blue line); the equilibrium temperature interpolated from the KMC curve is 1415K. (c): Evolution of the bulk Ge fraction obtained from the KMC run at T=1410K; the initial frames are discarded until the x_S value stabilises around a constant value (in this case, $\langle x_S \rangle$ =0.44, the standard deviation being $\sigma(x_S) = 0.04$ - see inset).*

The workflow of the calibration is described below:

- Set the calibration parameters α and β.
- Set the desired molar fraction of Ge in the liquid phase, x_L, which is assumed to be fixed during the KMC run and set to be equal to the initial solid seed (the latter assumption is arbitrary, since the composition of the solidified bulk material will depend on x_L and on the MC event probabilities).
- Run MulSKIPS in the temperature interval $[T_m^{exp} - 100, T_m^{exp} + 100]$, where T_m^{exp} is the equilibrium temperature in phase diagram, corresponding to $x = x_L$ (see **Figure 4a**). The equilibrium temperature, T_m^{KMC}, is interpolated as the temperature corresponding to zero interface velocity in the KMC runs (see **Figure 4b**).
- Run MulSKIPS at a constant temperature T^{run} slightly lower than T_m^{KMC}, to ensure quasi-equilibrium solidification of the material. In all the cases, we chose $T^{run} = T_m^{KMC} - 5\ K$.
- The Ge molar fraction of the solidified material, $x_S^{KMC} = \frac{n_{Ge}}{n_{Si}+n_{Ge}}$, and the standard deviation σ_S^{KMC}, are calculated by tracking the number of Si and Ge atoms solidified at every time frame in the KMC cycle, and averaging the Ge fraction once the solidification is stabilized (see **Figure 4c**). Similarly, the molar fraction of Ge at the surface of the material, x_{surf}^{KMC}, can be estimated from the count of the uncoordinated Si and Ge atoms (output xyz files from MulSKIPS), averaging from the same time steps.
- Compare the KMC results to the experimental phase diagram in **Figure 4a**.

The calibration has been validated by means of comparisons with the interface speed in Si and Ge as function of the under(over) cooling and the estimate of the solidus-liquidus region for the SiGe alloy.

4 Preliminary simulations of SiGe(001) LA processes

In this section, we present preliminary results of simulations performed with the new version of the code discussed in Section 2, for the case of an LA process of a SiGe (001) surface, under the assumption of homogeneous nucleation of the molten phase. We set up a CAD mesh as 20 μm-long along z and 10.8 nm large along x and y, containing a 19.8 μm thick SiGe layer with 200 nm air above it. The top 65 nm of SiGe was selected as the region to be mapped into the KMC superlattice, including also 4 nm of air within the KMC box. The resolution of the mesh in correspondence to the KMC region was set to 1 nm, and it gradually becomes coarser far from it.

The optical and thermal parameters for solid and liquid SiGe reported in **D4.1** and **D4.2** were used in the FEM calculations described in this section. It should be noted that these parameters were obtained for LA processes of relatively thin (roughly 30 nm) strained SiGe layers deposited on a much thicker Si substrate. However, the calculations presented here do not include a Si substrate in the mesh, but rather a clean unsupported strained SiGe sample is considered, with no misfit dislocations or other strain-relieving defects. The response of such homogeneous material to the laser irradiation is obviously very different from that of supported SiGe, hence the reported results (in terms of melt depth or Ge concentration profiles) cannot be quantitatively compared with experimental measurements carried out at similar laser energy densities. The presented calculations should be regarded as preliminary test studies, with the only objective of proving the correct implementation of the code's newly implemented features.

Another important approximation to keep in mind is that the Ge fraction in liquid, both in FEM and KMC frameworks, was fixed to a constant value of 0.6 throughout the whole LA process simulation. On-going implementation efforts in this regard will ensure that the FEM optical/thermal parameters for SiGe, as well as Si and Ge melting/solidification probabilities in KMC, will have a dependence on the space-time varying Ge fraction in the material. In particular, the Ge fraction in the liquid will be extracted *on-the-fly* within the KMC framework, used therein to update melting/solidification MC event probabilities (see **Equation 1**), and also passed to the Python environment, which will update the materials' thermal/optical properties accordingly. Anyways, no actual liquid atoms, nor Ge diffusion events in the liquid phase, will be modeled in the simulation. The LA tool presented here works in the limit of infinite Ge diffusivity in the liquid phase, such that an averaged value of Ge fraction in liquid is always assumed. This approximation can be deemed reasonable, given the small feature size of the systems that can be simulated.

In the KMC simulation setup, we consider a value of PtransZig=1.0 and an initial solid Ge fraction in SiGe of 0.25. The latter is close to the equilibrium solid Ge fraction corresponding to the considered liquid Ge fraction of 0.6. This choice guarantees a close-to-equilibrium environment during melting, given the imposed constraint of fixed liquid Ge fraction.

At the onset of laser irradiation (0 ns) the KMC cell contains 65 nm of solid SiGe and 4 nm of air, for a total of 268.150 Si sites and 89.450 Ge sites randomly arranged within the KMC solid system. The FEM simulates heating of the SiGe system induced by the laser pulse starting from a temperature of 300K, at time steps of 1 ns. Once the temperature reaches a threshold value of around 1523K, corresponding to a temperature slightly larger than the liquidus equilibrium temperature for SiGe with x_L=0.6 Ge fraction, the FEM-KMC hybrid calculation begins, the F2Py socket is initialized and the LA self-consistent simulation proceeds as outlined in **Figure 1**, at finer time steps of 0.5 ns (this guarantees good numerical accuracy, see **Deliverable D4.4, Figure 9**). To avoid early termination of the KMC cycle, possibly caused by the implemented stopping criterion based on the conservation of the original number of solid sites, we ensure a steady onset of melting by turning the top 0.5 nm of SiGe to liquid phase, all at once before the first KMC iteration. The melting front drops ~40 nm along z in roughly 90 ns since the beginning of melting. As expected, given the homogeneous nucleation and the close-to-equilibrium state of the alloy, the solid-liquid interface remains quite flat for the whole simulation, also during the later solidification. Remarkably the expected Ge segregation, due to the different kinetics of Ge and Si atoms in the SiGe alloy, was successfully captured by our simulations. Moreover, during solidification, a few point defects could also be generated and retained during the LA simulation, because of the new functionalities offered by F2Py sockets.

In particular, **Figure 5a** shows the variation over time of the maximum and minimum temperature in the mesh subregion modeled with KMC. After the initial, almost linear, heating phase, the expected sharp discontinuity in the slope of maximum temperature at around 80 ns can be noted, due to the abrupt change in thermal conductivity and surface reflectivity between solid and liquid SiGe, the latter being present as a uniform 0.5 nm thick uniform layer on top of the structure as soon as melting sets off. The comparison with the minimum temperature profile (dashed line) shows that the gradient of temperature initially existing between the bottom and top of the KMC subregion gradually decreases with simulation time. It can be seen that a quite linear cooling trend begins at around 200 ns, due to the reduction in laser power (the pulse duration was 160 ns), causing a steady resolidification of the material.

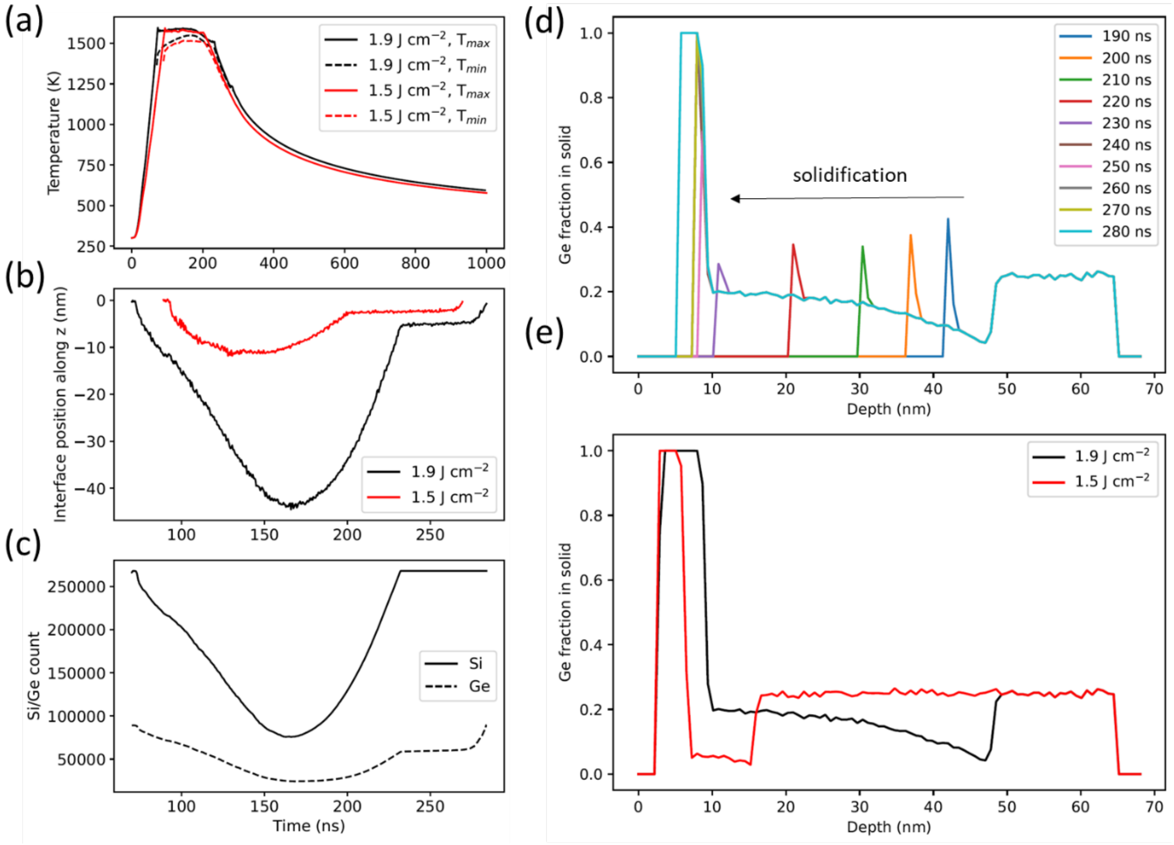

Figure 5 - Analysis of an LA simulation for $SiGe_{0.25}$ at two laser pulse energy densities, namely 1.9 J cm^{-2} (black) and 1.5 J cm^{-2} (red). (a) The maximum and minimum temperature in the mesh subregion coupled with KMC. (b) Melt depth profile vs. time. (c) Count of solid Si and Ge atoms during the simulation time interval where FEM is coupled with KMC, for the 1.9 J cm^{-2} fluence. (d) Ge concentration in solid as a function of depth (surface is on the left) at various instants during solidification. (e) Final Ge concentration profile after solidifications for the two considered fluences.

The latter can also be inferred from the profiles of melt depth vs. time reported in **Figure 5b**, computed as the average z coordinate of all undercoordinated solid atoms in the KMC box, as well as from the count of solid Si and Ge sites in the KMC box during the KMC cycle, reported in **Figure 5c**. Both **Figure 5b-c** also show very clearly that Si atoms solidify faster than Ge (as expected, given the different melting temperatures of pristine Si and Ge), and that at some point a quasi-stable situation is achieved (plateaus in **Figure 5b-c**), where the solid interface with liquid stands still for roughly 50 ns. This almost stationary situation takes place because, in this time interval, the temperature is still quite higher than the melting temperature of pristine Ge (1210K). To a minor extent, this may also be due to the few residual Si atoms at the interface with liquid which tend to solidify with a probability that does not account for the much higher concentration of Ge in the liquid phase existing at this point in the LA process. The latter effect is an artificial consequence of keeping the Ge concentration fixed in the FEM parameterization and in the KMC calibration (see discussion above) and will be fixed once this constrain will be relaxed in the next code developments. Once the initial number of solid Si atoms is totally recovered, and the temperature drops around 1210K, Ge atoms undergo rapid solidification, detectable in **Figure 5a** as a tiny kink in the temperature profile, and the system slowly releases the accumulated heat, thermalizing to room temperature after several ms from the end of irradiation.

Thanks to the new tracking features enabled by the usage of F2Py sockets, it is also possible to extract the profile of Ge concentration as a function of depth in the solidified system, at any instant of the LA simulation. Such type of information can be extremely useful to interpret SIMS or STEM-EDX Ge profiles measured after an LA process and understand the kinetic mechanisms which lead to the final surface morphology and bulk composition of an LA processed SiGe sample. For instance, **Figure 5d** shows how this concentration profile evolves over 90 ns since the beginning of solidification, while **Figure 5e** shows the final profile as a function of depth. Interestingly, this profile shows a gradual increase in Ge concentration in the solidifying material due to segregation, a feature generally found also experimentally, and also confirms the maximum melt depth already inferred from **Figure 5b**.

Lastly, as a further technical and qualitative check of the code's correct functioning, in **Figure 5** we also report the results of an LA simulation carried out for a lower value of laser fluence, namely 1.5 J cm^{-2}. As expected, due to the lower absorbed thermal budget, we find that the temperature raises with a smaller slope (see **Figure 5a**) and a smaller maximum melt depth is achieved (see **Figure 5b**), with less Ge segregation on top of the final surface (see **Figure 5e**).

Conclusions

This deliverable has deployed the full potentiality of the laser annealing module of the MulSKIPs code, comprising the possibility to simulate with an atomic resolution the formation of defects and complex geometries during the LA process of group IV semiconductors and alloys. This goal has been achieved through the formulation of hybrid theoretical models that couple continuum fields to atomistic simulation schemes (KLMC here) and their implementation in a single computational code through advanced software engineering procedures (including communicating Fortran and Python modules, RAM sharing, sockets, etc.). The complete theoretical/computational methodology can now be fully applied to advanced materials with a non-definite stoichiometry (e.g. to SiGe alloys). Here, a first calibration for the solid/liquid interface of SiGe alloys with variable alloy fractions as well as examples of laser annealing in SiGe has been deployed. The final version of all LA models as well as relevant examples will be described in Deliverable D4.8.

References

1. **A. La Magna, P. Alippi, V. Privitera, G. Fortunato, M. Camalleri, B. Svensson.** A phase-field approach to the simulation of the excimer laser annealing process in Si. *Journal of Applied Physics.* AIP, 2004, Vol. 95, 9, p. 4806.

2. **S.F. Lombardo, G. Fisicaro, I. Deretzis, A. La Magna, B. Curver, B. Lespinasse, K. Huet.** Theoretical study of the laser annealing process in FinFET structures. *Applied Surface Science.* Elsevier, 2019, Vol. 467–468, 666-672.

3. **G. Calogero, D. Raciti, P. Acosta-Alba, F. Cristiano, I. Deretzis, G. Fisicaro, K. Huet, S. Kerdilès, A. Sciuto, A. La Magna.** Multiscale modeling of ultrafast melting phenomena. *npj Computational Materials.* Nature Publishing Group, 2022, Vol. 8, 36.

4. **Kenneth A. Jackson, George H. Gilmer, Dmitri E. Temkin.** Monte Carlo Simulation of the Rapid Crystallization of Bismuth-Doped Silicon. *Phys. Rev. Lett. .* 1995, Vol. 75, 2530, p. 2530 .

5. **La Magna, A., et al.** Vacancy generation in liquid phase epitaxy of Si. *Physical Review B.* APS, 2007, Vol. 75, 235201, p. 235201.

6. **Woodraska, Donald L. e Jaszczak, John A.** A Monte Carlo simulation method for {111} surfaces of silicon and other diamond-cubic materials. *Surface science.* Elsevier, 1997, Vol. 374, p. 319-332.

7. **Stiffler, S. R., Evans, P. V. e Greer, A. L.** Interfacial transport kinetics during the solidification of silicon. *Acta metallurgica et materialia.* 1992, Vol. 40, p. 1617-1622.

8. **La Magna, A., et al.** Simulation of the Growth Kinetics in Group IV Compound Semiconductors. *Phys. Status Solidi A.* 2019, Vol. 216, 1800597.

9. **Mittiga, A., Fornarini, L. & Carluccio, R.** Numerical modeling of laser induced phase transitions in silicon. *Appl. Surf. Sci.* 2000, Vol. 154-155, 112-117.

10. **R. W. Cahn, P. Haasen.** *Physical Metallurgy.* Amsterdam : Elsevier Science, 1996. 9780080538945.

11. **Pelton, A. D.** Thermodynamics and phase diagrams of materials. *Phase transformations in Materials.* 2001, 1-80.

12. **Kaptay, George.** On the solid/liquid interfacial energies of metals and alloys. *Journal of Materials Science.* 2018, Vol. 53, 3767–3784.

13. **Butler, John A. V.** The thermodynamics of the surfaces of solutions. *Proc. R. Soc. A.* 1932, Vol. 135, 348-375.